Modeling of secondary emission processes in the negative ion based electrostatic accelerator of the International Thermonuclear Experimental Reactor

G. Fubiani, H. P. L. de Esch, and A. Simonin*

DSM/DRFC, Association EURATOM-CEA, CEA Cadarache, F-13108, St. Paul lez Durance, France

R. S. Hemsworth

ITER Joint Work Site, CEA Cadarache, F-13108, St. Paul lez Durance, France

(Received 19 October 2007; published 8 January 2008)

The negative ion electrostatic accelerator for the neutral beam injector of the International Thermonuclear Experimental Reactor (ITER) is designed to deliver a negative deuterium current of 40 A at 1 MeV. Inside the accelerator there are several types of interactions that may create secondary particles. The dominating process originates from the single and double stripping of the accelerated negative ion by collision with the residual molecular deuterium gas ($\simeq 29\%$ losses). The resulting secondary particles (positive ions, neutrals, and electrons) are accelerated and deflected by the electric and magnetic fields inside the accelerator and may induce more secondaries after a likely impact with the accelerator grids. This chain of reactions is responsible for a non-negligible heat load on the grids and must be understood in detail. In this paper, we will provide a comprehensive summary of the physics involved in the process of secondary emission in a typical ITER-like negative ion electrostatic accelerator together with a precise description of the numerical method and approximations involved. As an example, the multiaperture-multigrid accelerator concept will be discussed.

DOI: 10.1103/PhysRevSTAB.11.014202 PACS numbers: 29.20.−c

I. INTRODUCTION

The 1 MeV, multi-MW, neutral beam (NB) injectors [1] are required for plasma heating and current drive in the future fusion machines such as the International Thermonuclear Experimental Reactor (ITER) [2]. In the case of ITER, the NB injector is designed to deliver 1 MeV, 17 A (equivalent) of neutral deuterium atoms (i.e., 17 MW of power) to the ITER plasma. The device is mainly composed of a negative deuterium ion source delivering a current density of the order of 28 mA/cm^2 to an electrostatic accelerator producing a 1 MeV, 40 A D^- beam, a neutralizer which converts part of the beam into high energy neutrals [3], and a residual ion dump.

This paper will focus on the physics related to particle-particle and particle-surface interactions inside a multiaperture-multigrid–type of negative ion accelerator [1,4]. Such an accelerator consists of a plasma grid (PG), an extraction grid (EG), and a series of acceleration grids (AG). A schematic representation of the accelerator is shown in Fig. 1. The D^- ion source is directly connected to the plasma grid. Negative ions arriving at an aperture in the plasma grid are extracted from the plasma inside the source by applying an electric field between the extraction grid and the plasma grid. The extracted ions pass through the apertures in the extraction grid and electric fields between each of the subsequent acceleration grids accelerate the ions to the desired energy through similar apertures in each acceleration grid. The interactions considered are mainly secondary particle production processes, principally: (i) coextracted electrons from the negative ion source, (ii) negative ion stripping inside the accelerator vessel by collisions with the residual gas, and (iii) ionization of the latter. The secondary particles produced (which include electrons and heavy particles such as neutrals and positive ions) follow a path determined by the electric and magnetic fields inside the accelerator and may, in turn, cause more secondary particle production by direct impact on the extraction and acceleration grids. Short range magnetic fields generated by permanent magnets

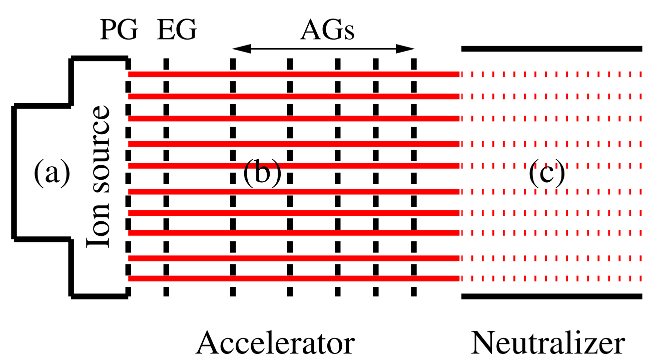

FIG. 1. (Color) Schematic representation of a multiaperture-multigrid–type negative ion accelerator. Neighboring components of the neutral beam injector are also shown for clarity. In region (a), the negative ion source, region (b), a five-stage electrostatic accelerator, and region (c), the neutralizer. Accelerated negative ion beamlets are shown in red. They are gradually neutralized inside the neutralizer.

*alain.simonin@cea.fr

embedded in the extraction grid deflect coextracted plasma electrons onto the extraction grid [3], while having little effect on the trajectories of the heavier D^- ions. With the ion source designed for ITER, long range magnetic fields are produced by passing a few kA current through the plasma grid and the field from permanent magnets on the source itself.

The overall power deposition due to energetic secondary particles hitting the grids may be of the order of a few MW and consequently a precise understanding of its origin and location inside the accelerator cavity is required for design improvement.

In this paper, the work is completely theoretical. We will describe in detail the numerical code which was developed to accurately describe secondary emission issues in typical electrostatic accelerators and, as an example, we will fully simulate the Japanese multiaperture-multigrid (MAMuG) accelerator [1,4] designed for ITER. This consists of an extraction system and a five-stage electrostatic accelerator where each stage provides 200 keV of energy gain to the negative ions.

The paper is organized as follows: Sec. II gives a detailed description of the electrostatic accelerator Monte Carlo code (EAMCC[1]). The code tracks test macroparticles inside the accelerator; collisions with grids and residual background gas are calculated using the conventional Monte-Carlo technique [5]. In Sec. III, the simulation of the MAMuG accelerator is described, showing calculation of power deposition and current on accelerator grids induced by particle impacts, i.e., from coextracted plasma electrons, by-products of negative ion stripping reactions, ionization of background gas, and associated secondary particles generated by these processes. We also include scenarios with a highly divergent fraction of the beam within the negative ion beam, hereinafter referred to as the "halo." In the EAMCC code the halo formation is assumed to arise from ions created on the downstream surface of the plasma grid. Cesium (Cs) is injected into the ion source to lower the work function of metal surface [6], which is found to enhance the negative ion yield. Cs will migrate out of the ion source to the back of the plasma grid, inside the accelerator. Neutral atoms leaving the ion source may impinge on that surface and create negative ions. The ions can form a non-negligible halo (on the order of 5%–15% of the accelerated beam current [7]). Halos in general will substantially increase power deposition due to direct impact of the negative ions on the accelerator grids.

II. DETAILED DESCRIPTION OF THE NUMERICAL APPROACH

EAMCC is a 3-dimensional (3D) relativistic particle tracking code where macroparticle trajectories, in prescribed electric and magnetic fields, are calculated inside the accelerator vessel. In the code, each macroparticle represents an ensemble of rays (carrying a microcurrent of typically $\simeq 50$ nA).

The electric field map is obtained from the code SLAC-CAD [8] that solves Poisson's equation on a 2D cylindrically symmetric grid. SLAC-CAD does not perform any plasma physics calculations. Consequently, the plasma meniscus, which separates the source plasma from the accelerated negative ion beam, is calculated rather simply by imposing a vanishing electrostatic field inside the simulation domain dedicated to the ion source area, i.e., the region where the potential drops below the plasma grid potential.

The magnetic field from a set of SmCo permanent magnets is calculated following a semianalytical approach [9] while the field from the $\simeq 4$ kA circulating through the plasma grid of the ITER accelerator is performed assuming an infinitely thin electron sheath (e.g., a surface current) [10].

Collisions are described using a Monte-Carlo method [5]. The several kinds of collisions considered in the code are: (i) electron and heavy ion/neutral collisions with accelerator grids, (ii) negative ion single and double stripping reactions, and (iii) ionization of background gas.

A. Electron impact on accelerator grids

Particle impact with grids may have different origins. The greatest power deposition is from electrons. As mentioned earlier, electrons may originate from the ion source plasma (we assume one electron is extracted per negative ion extracted [11,12]). These are deflected by the magnetic fields in the accelerator, which, in the extraction gap, comes mainly from the magnets embedded in the extraction grid (EG). The second most significant source of electrons is stripping of the extracted negative ions via collisions with the background gas. Electrons produced between the accelerator grids (AG) are accelerated to high energy.

Heavy ions and neutrals also impact on the grids. The majority of such impacts are from high divergence neutrals created in the gap between the plasma grid and the first acceleration grid and consequently are from particles with a relatively low energy. Most neutrals and a large fraction of ions created after the extraction grid are either transmitted out of the accelerator, or accelerated back to the ion source (only positive ions H_x^+ or D_x^+, where $x = 1$ or 2).

Modeling the consequences of electron impacts with accelerator grids requires the knowledge of the energy and spatial distribution of secondary and reflected electrons. These depend mainly on the incident electron energy and angle [13–16]. Secondary electron energy emission spectra may be separated into three quasi-independent phenomena [17]: (i) true secondary electron production with a typically low-energy spectra extending from 0 to 50 eV; (ii) backscattered electrons with an energy range 0

[1] A copy of the code is available on demand.

to E_0, where E_0 is the energy of the incident electron; and (iii) elastically reflected electrons with $E_{k_b} \simeq E_0$, where E_{k_b} is the reflected electron energy, i.e., electron reflection with almost no energy loss. The latter effect is negligible for energies greater than $\simeq 500$ eV [16] and it is not included in EAMCC.

The modeling of backscattered electron processes is based on a semianalytical approach. The backscattered integrated electron energy spectra is assumed to be [18]

$$\eta(\hat{E}) = S \exp\left[-\left(\frac{K}{1-\gamma\hat{E}^{\alpha}}\right)^{p}\right], \tag{1}$$

where $\hat{E} = E_{k_b}/E_0$ is the normalized backscattered electron kinetic energy,

$$S = \eta_{b0} \exp(K^p), \tag{2}$$

$\eta_{b0} \equiv \eta(\theta_1 = 0)$ is the probability for a primary electron to be backscattered at normal incidence,

$$\gamma = 1 - \exp[-6|\ln B_\theta|^{-3/2}], \tag{3}$$

$$K = 70|\ln B_\theta|^4, \tag{4}$$

and

$$B_\theta(E_0, \theta_1, \theta_2) = B_0 \prod_i^2 \exp[\tau(1-\cos\theta_i)]. \tag{5}$$

In Eqs. (1)–(5), the independent variables p, B_0, α, and τ are parameters used to fit experimental data taken for Matsukawa *et al.* [14] for incident electron energies of 10 and 20 keV and from Sternglass *et al.* [16] for 2 and 370 keV, respectively. Negligible variations are assumed for $\eta(\hat{E})$ below 2 keV and above 370 keV [16]. For intermediate energies, a linear interpolation is performed to deduce $p(E_0)$, $B_0(E_0)$, $\alpha(E_0)$, and $\tau(E_0)$. Table I summarizes the fitting values used in EAMCC; note that $\alpha = 2.2$ is found for all energies.

Furthermore, it has been shown by Matsukawa *et al.* [14] that the peak value of the backscattered electron energy spectra moves toward high energy ratios $\hat{E}$ for increasing angle of incidences θ_1 and scattering angles θ_2. It is expected to get a maximum value at grazing incidence and scattering, i.e., for $\theta_1 = \theta_2 = \pi/2$. Equation (5) is included in EAMCC to accurately model this effect. The fitting parameter $\tau(E_0)$ is calculated assuming

$$B_\theta(E_0, \pi/2, \pi/2) = \Omega, \tag{6}$$

TABLE I. Fitting parameters deduced from experimental measurements found in Refs. [14,16].

E_0 (keV)	2	10	20	370
B_0	0.2	0.24	0.265	0.273
p	0.32	0.27	0.27	0.27
τ	0.51	0.412	0.365	0.35

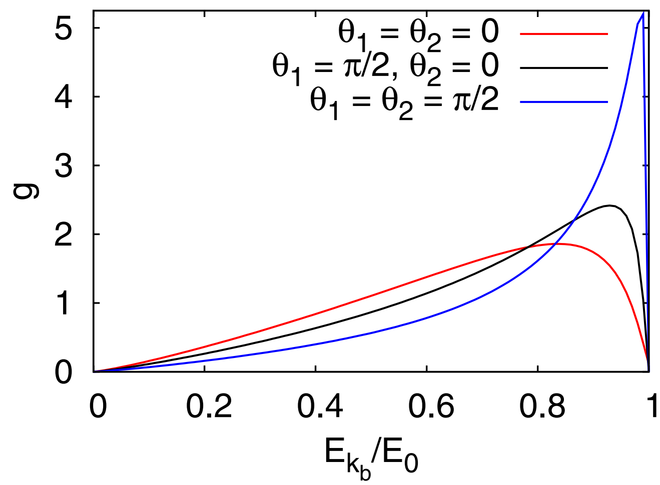

FIG. 2. (Color) Backscattered electron energy spectra $g(\hat{E}) = -d\eta/d\hat{E}$ as a function of $\hat{E} = E_{k_b}/E_0$ for $E_0 = 20$ keV and three values of incidence and scattering angles θ_1 and θ_2. We observe the peak value of the spectra moving toward high energy ratios $\hat{E}$ for increasing values of θ_1 and θ_2.

where the value $\Omega = 0.55$ was chosen based on measurements reported in Ref. [14]. Figure 2 shows the backscattered electron energy spectra $g(\hat{E}) = -d\eta/d\hat{E}$ as a function of $\hat{E} = E_{k_b}/E_0$ for $E_0 = 20$ keV and three values of incidence and scattering angles θ_1 and θ_2.

Last, in EAMCC the energy of a backscattered primary electron is obtained by normalizing and inverting Eq. (1) giving

$$\frac{E_{k_b}}{E_0} = \left\{\frac{1}{\gamma}\left[1 - \frac{K}{\ln^{1/p}(S/P)}\right]\right\}^{1/\alpha}, \tag{7}$$

where P is a random number between 0 and 1.

The probability for a primary electron impacting the grid at an incidence angle θ_1 to be backscattered is modeled using the well-known expression [15,18,19],

$$\eta_b(\theta_1) = \eta_{b0} \exp[A_{b0}(1-\cos\theta_1)], \tag{8}$$

where η_{b0} is the backscattered probability at normal incidence and the coefficient $A_{b0}(E_0)$ is obtained by fitting experimental data [18], giving

$$A_{b0} = \kappa(E_0) \ln(1/\eta_{b0}), \tag{9}$$

with

$$\kappa = 1 - \exp(-1.83 E_{0(\mathrm{keV})}^{1/4}). \tag{10}$$

In EAMCC, a backscattered electron is reemitted in the simulation from the location at which the primary electron impacted the grid and in an arbitrary direction $\{\theta_2, \phi\}$, where $\theta_2 \in [0, \pi/2]$ and $\phi \in [0, 2\pi]$ are obtained using a random number. This assumes an isotropic scattering of the backscattered particle (i.e. no preferred direction as a function of incoming angle θ_1), which is a good approximation in the sense that diffusion in velocity space is significant when more than a couple of collisions occur for the primary electron inside the grid material [20] (the latter argument is very likely to be true for high energy incident particles).

The backscattered probability at normal incidence η_{b0} on a copper target is taken from the ORNL Redbooks [21] in the energy range from 0.5 to 100 keV (giving a value close to $\eta_{b0} \simeq 0.3$). Later measurements in the range of 0.6–6 keV from Ref. [22] confirm the Redbook data [21]. Data for 1–12 MeV are available from Ebert *et al.* [23] and Wright *et al.* [24]. Furthermore, data from Wang [25] have been used to cover the energy range between 100 keV and 1 MeV. Lastly, extrapolation using Mo and Ag is used to obtain coefficients for energies of 100–500 eV [21]. Figure 3 shows η_{b0} for the energy range most relevant to NB injection devices, i.e., 100 eV to 1 MeV.

The true secondary emission yield (SEY) induced by primary electrons impacts on grids is described in a similar manner as for the case of backscattering, that is,

$$\eta_s(\theta_1) = \eta_{s0} \exp[A_{s0}(1 - \cos\theta_1)], \tag{11}$$

where $\eta_{s0}(E_0)$ is the SEY coefficient at normal incidence ($\theta_1 = 0$). For copper, data found from Refs. [26,27] are implemented in EAMCC. $A_{s0}(E_0)$ is the coefficient associated with the angle dependency of true secondary emission yield. Values for the energy range 0.5–10 keV are obtained by fitting experimental data found in Ref. [13] for copper targets. Because of the lack of reliable information for $E_0 < 0.5$ keV and $E_0 > 10$ keV, constant values for $A_{s0}(E_0 < 0.5\ \text{keV}) = A_{s0}(E_0 = 0.5\ \text{keV})$ and $A_{s0}(E_0 > 10\ \text{keV}) = A_{s0}(E_0 = 10\ \text{keV})$ are assumed. η_{b0} and A_{s0} are shown in Fig. 3 for the energy range relevant to NB injectors.

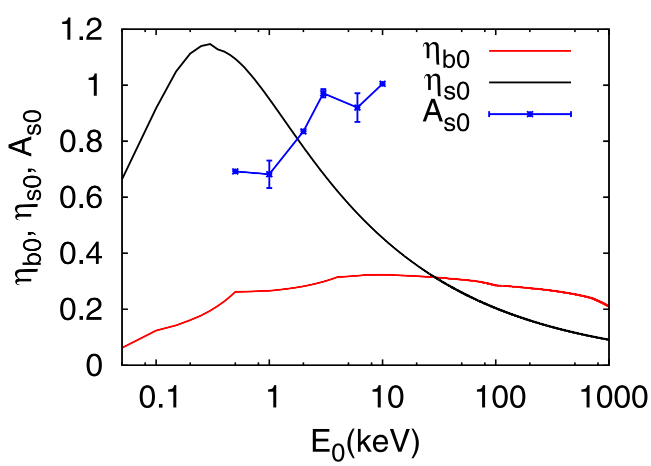

FIG. 3. (Color) Backscattered coefficient η_{b0} (red), secondary emission yield η_{s0} (black), and coefficient A_{s0} (blue), which describes the angle dependency of true secondary emission yield, are shown for a primary electron with energy E_0 (keV) impacting a copper target at normal incidence $\theta_1 = 0$.

Last, true secondary electron energy spectra are typically low energy (0–50 eV) and have a bell-like shape. In EAMCC, the energy of a true secondary electron produced at the grid surface is simply assumed to be constant ($E_0 =$ 10 eV) because that energy may be considered negligible compared to the particle energy gain once accelerated by the electrostatic field inside the accelerator vessel.

B. Negative ion stripping inside the accelerator downstream of the extraction grid

Stripping of negative ions (the loss of one or more electrons by collisions) is the main cause of high energy electron production in conventional electrostatic accelerators found on fusion machines (typically of the order of 20%–30% losses). These electrons are assumed to be emitted at the location of the collision with the same direction and velocity as the parent D^-. They will be accelerated by the electric field of the accelerator and deflected by less intense magnetic fields than found in the extraction area. This implies a larger Larmor radius and consequently a longer path inside the accelerator vessel before being intercepted (i.e., a higher energy gain).

Note that most of the coextracted plasma electrons are collected by the extraction grid ($\simeq 98\%$), which corresponds to a relatively low power deposition ($\simeq 500$ kW for the accelerator of the ITER NB injector) due to the moderate potential difference between the plasma and extraction grid ($\simeq 9$ kV).

Negative ion stripping occurs due to collisions with the residual background gas in the accelerator which either comes from the ion source or the neutralizer.

The main reactions leading to destruction of negative hydrogen ions and production of secondary particles considered in EAMCC are summarized in Table II and are shown in Fig. 4. For deuterium ions, we use the same cross sections as for the case of hydrogen for identical particle velocities ($v_H = v_D$). The cross section for the ionization of H_2 by H^-, i.e., reaction 3, is assumed to be equal to that of the ionization by H^0 over the energy range of interest, 10 keV to 1 MeV. This is true for $E_0^{(H)} \leq 50$ keV [29]. The extrapolation to higher energies is justified as the plane wave Born approximation predicts that for $E_0^{(H)} >$ 1.5 MeV the cross section should be equal to that of H^+,

TABLE II. Major processes involved in the destruction of negative hydrogen ions and production of secondary particles inside the accelerator vessel [28].

Reaction number	Process	Label
1	$H^- + H_2 \rightarrow H^0 + H_2 + e^-$	Single stripping
2	$H^- + H_2 \rightarrow H^+ + H_2 + 2e^-$	Double stripping
3	$H^- + H_2 \rightarrow H^- + H_2^+ + e^-$	Ionization
4	$H^0 + H_2 \rightarrow H^0 + H_2^+ + e^-$	Ionization

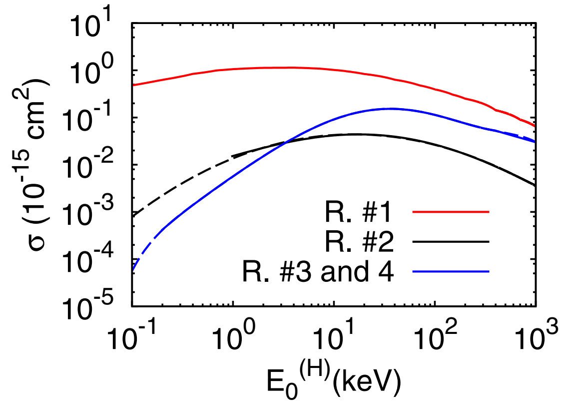

FIG. 4. (Color) Cross sections for production of secondary particles inside the accelerator vessel due to the interaction between the accelerated negative ions and residual background gas (H_2 or D_2) are shown for the case of hydrogen (solid lines). Reactions 1 to 4 are displayed in Table II. The cross sections for deuterium are found assuming $E_0^{(D)} = 2E_0^{(H)}$. The dashed lines correspond to the numerical fit implemented into EAMCC. Concerning the ionization of background gas (H_2 or D_2) by negative ions (H^- or D^-) or neutrals (H^0 or D^0), we assume the same cross section for both reactions [29].

which is slightly greater than that of H^0 at lower energies [28].

In EAMCC, reactions 1–4 of Table II are calculated using a Monte-Carlo method [5]. For instance, the rate equation for destruction of negative ions may be written as follows:

$$\frac{dN_-}{dz} = -\sum_{i=1}^{2} \nu_i(z)N_-, \qquad (12)$$

giving

$$N_-(z) = N_{0-} \exp\left[-\int_0^z \nu_{\mathrm{tot}}(z)dz\right], \qquad (13)$$

where $N_-(z)$ is the number of negative ions at location z inside the accelerator, $N_{0-} = N_-(0)$ is the number at extraction (plasma grid location),

$$\nu_{\mathrm{tot}}(z) = n_g(z)\sum_{i=1}^{2} \sigma_i(z)$$

is the total frequency associated with reactions 1 and 2; n_g is the background gas density.

Consequently, one considers that a reaction occurred for a macroparticle if within a small interval Δz we have

$$r_1 \leq \frac{\Delta N_-(z_i)}{N_-(z_i)} = 1 - \exp[-\nu_{\mathrm{tot}}(z_i)\Delta z], \qquad (14)$$

where $\Delta N_-(z_i) = N_-(z_i) - N_-(z_i + \Delta z)$ and r_1 is a random number between 0 and 1. In order to determine which type of reactions occurred (1 or 2), a second random number r_2 is used. If $r_2 \leq \nu_1/\nu_{\mathrm{tot}}$ then reaction 1 occurred, otherwise reaction 2 would have happened.

The same reasoning is applied to the ionization of the background gas (H_2/D_2) by collisions with negative ions (H^-/D^-) and neutrals (H^0/D^0) (reactions 3 and 4).

Note that, in a general manner, if a particle was involved in more than two reactions, say k for instance, then reaction 1 will occur if $r_2 \leq \nu_1/\nu_{\mathrm{tot}}$, reaction 2 will occur if $r_2 \leq (\nu_1 + \nu_2)/\nu_{\mathrm{tot}}$, reaction $(k-1)$ will occur if

$$r_2 \leq \nu_{\mathrm{tot}}^{-1}\sum_{i=1}^{k-1} \nu_i,$$

where

$$\nu_{\mathrm{tot}} = \sum_{i=1}^{k} \nu_i.$$

In EAMCC, trajectories for each newly created electron, ion, or neutral are followed together with all collision processes that may occur for those macroparticles (collisions with background gas molecules, impact with grids, etc.).

We assume that the neutral atoms and positive ions created via reactions 1 and 2 of Table II, have initial velocities identical to that of their precursor negative ions, meaning $v_0 = v_-$ and $v_+ = v_-$, where v_0 and v_+ are the atom and positive ion velocities, respectively. Electrons are assumed to be emitted at rest in the center of mass frame, i.e., $v_e = v_-$ and $E_0^{(e)} = (m_e/m_-)E_0^{(i)}$, where m_- and m_e are the negative ion and electron mass, respectively (it is to be noted that when electrons are accelerated to high energy their mass is corrected for the relativistic effect).

Concerning reactions 3 and 4 of Table II, the kinetic energies of the hydrogen/deuterium molecules is negligibly small $T_i \lesssim 0.2$ eV ($\simeq 2000$ K) compared to the energy gain of these particles once accelerated by the electric field in the accelerator vessel. Consequently, electrons and positive molecular ions (H_2^+ or D_2^+) are assumed to be created at rest in the laboratory frame.

C. Heavy particle impact with accelerator grids

Heavy ions or neutrals induced by background gas ionization or negative ion stripping may themselves undergo collisions with the gas or impact with the accelerator grids. Positive ions usually either go back toward the ion source or impact the back of a grid (the front of a grid is defined as facing the ion source). Heavy ion or neutral impacts with the grids may in turn result in the creation of secondary electrons together with the possibility of being backscattered. Because of their larger stopping power, the SEY may be significantly greater than the one induced by primary electron impacts.

A complete description of ion impacts with copper surfaces needs the integration into the physical model of the energy spectrum of the backscattered particles. Simulations performed with EAMCC show that rediffused ions after impinging a grid amount for a negligible ratio of the total number of ions created in the accelerator vessel, typically $\simeq 4.5\%$ for D_2^+, $\simeq 5.5\%$ for D^+, and $\simeq 8.5\%$ for D^0 in the Japanese MAMuG concept [1,4]. Furthermore, the power deposited on grids by ions and neutrals remains small compared to that from electrons, i.e., $\simeq 4\%$ of the total power. Consequently, a simplified description of the physics associated with ion and neutral backscattering (energy spectra, incidence angle dependency, etc.) is implemented in the algorithm. Note that backscattering may be a negligible effect but, on the contrary, true secondary electron emission induced by heavy particle impacts is not. It is essential to describe accurately the latter effect.

The SEY from proton and molecular hydrogen ion (H_2^+) impacts at normal incidence ($\theta_1 = 0$) is modeled using data from Refs. [21,30,31]. The maximum yield for protons is found to be $\eta_{s0}^{(+)} \simeq 1.32$ (shown in Fig. 5) and $\eta_{s0}^{(2)} \simeq 2.9$ for H_2^+. In addition, the SEY ratio $\eta_{s0}^{(2)}(v_2)/\eta_{s0}^{(+)}(v_+)$ is assumed constant for identical incident particle velocities, that is $v_+ = v_2$ [30,31]. The latter statement is approximately true for energies $E_0^{(+)} \gtrsim 100$ keV, which is the relevant energy range for ions that impact the grids in a typical ITER-like electrostatic accelerator.

Similar reasoning is applied to D^+ and D_2^+. For instance, there is substantial evidence that coefficients for H^+ and D^+ are the same at equal velocities [21,31].

Last, we assume identical SEYs from neutrals H^0 or D^0, negative ions H^- or D^-, and positive ions H^+ or D^+, which are impacting on the grids [21], that is $\eta_{s0}^{(0)}(E_0) \sim \eta_{s0}^{(-)}(E_0) \sim \eta_{s0}^{(+)}(E_0)$.

In addition, the corresponding angular dependency is calculated using the same expression as in Eq. (11), that is

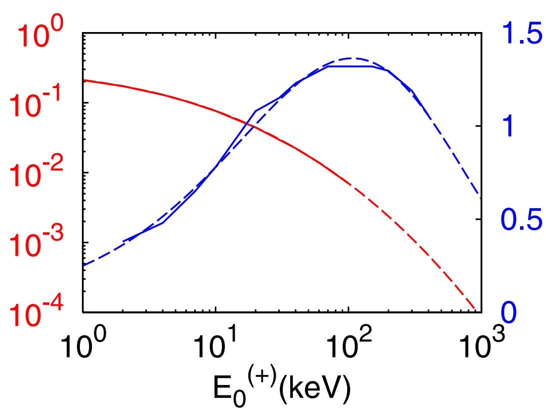

FIG. 5. (Color) Proton backscattering coefficient η_{b0}^{ion} (red) and true secondary emission yield induced by proton impacts on copper targets, $\eta_{s0}^{(+)}$ (blue), is shown as a function of incident ion kinetic energy $E_0^{(+)}$ (keV) and at normal incidence ($\theta_1 = 0$). Cross sections for heavier ions (H_2^+, D^+, etc.) are assumed to be similar at equal incident velocities. Dashed lines correspond to the numerical fit implemented into EAMCC.

$$\eta_s^{(i)}(\theta_1) = \eta_{s0}^{(i)} \exp[A_{s0}^{(i)}(1 - \cos\theta_1)], \tag{15}$$

where the parameter $A_{s0}^{(i)}$ was found to be close to 1.45 based on data taken from Ref. [21]. The latter corresponds to measurements for protons impacting Ni targets. Because of the lack of information on copper, in EAMCC it is assumed that the same value of $A_{s0}^{(i)} \equiv A_{s0}^{\mathrm{ion}}$ applies to copper targets and for all heavy particle impacts (i.e., heavy ions and neutrals).

Concerning secondary electron energy spectra and following the discussion of Sec. II A, we again assume electrons are emitted at a fixed energy, that is $E_0 = 10$ eV. The energy range is typically found to be between 0–50 eV [21].

Backscattering of heavy ions and neutrals off a grid is modeled according to data found in [21]. The particle reflection coefficient is shown in Fig. 5. For the angular dependence, we use a cosine law of the form

$$\eta_b^{\mathrm{ion}}(\theta_1) = \frac{\eta_{b0}^{\mathrm{ion}}}{(1 - \mu)\cos\theta_1 + \mu}, \tag{16}$$

where μ is a free parameter currently set to $\mu = 1/2$ which defines a backscattering probability at grazing incidence twice as high as for the case of normal incidence. Note that the same coefficient $\eta_{b0}^{\mathrm{ion}}(E_0)$ is used for all types of heavy particles. Furthermore, the same reasoning is applied to describe average backscattered ion energy as a function of incident angle.

In addition, a backscattered ion may suffer a change of charge state [21]. It is typically found that for proton impacts the backscattered particles are predominantly neutrals ($\simeq 100\%$–85% for backscattered energy ratios $\hat{E} = E_{k_b}/E_0$ ranging between 0 and 1), followed by positive ions ($\simeq 0\%$–13%), and lastly negative ions ($\simeq 0\%$–5.5%). Implementation of the latter effect needs the inclusion of the backscattered particle energy spectrum. In EAMCC, we use an average profile taken from [32].

III. APPLICATIONS

We apply the numerical method described in Sec. II to the calculation of secondary emission processes in the ITER multiaperture-multigrid (MAMuG) electrostatic accelerator concept [1,4]. As previously mentioned, MAMuG is a five-stage accelerating device. The geometry of the MAMuG accelerator is shown in Fig. 6. Each stage corresponds to a copper grid with a total number of 1280 holes. The transverse size of a grid is of the order of 0.8×1.5 m^2, corresponding to a significantly higher cross-sectional area compared to other ion accelerators. Each of the 1280 negative ion beamlets is accelerated through one of the grid holes, gaining 200 keV between two successive acceleration grids (AG). Figure 6 shows one beamlet. The first grid (left side) corresponds to the PG, the second one is the extraction grid (EG) which is, in this

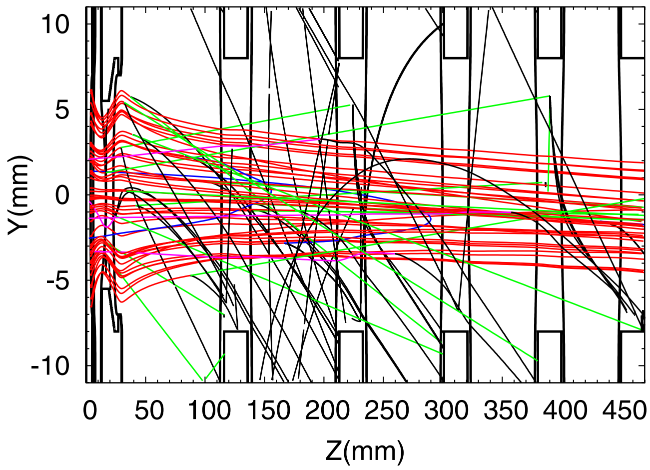

FIG. 6. (Color) Geometry of the MAMuG negative ion based electrostatic accelerator. The plot shows a zoom over one beamlet. From left to right: plasma grid (PG), extraction grid (EG) (at an extraction voltage of 9.4 kV), and acceleration grids (AG) 1 through 5 (total acceleration voltage of 1 MV). Primary and secondary particles are shown; negative deuterium ions (red color), neutrals (D^0) (green), positive deuterium ions (D^+) (blue), positive deuterium molecular ions (D_2^+) (purple), and electrons (black). The negative ion beam aims downward with an average divergence $\langle y' \rangle \simeq 5.5$ mrad induced by the PG magnetic filter field (generated by a 4 kA current).

configuration, at an extraction potential of 9.4 kV. Last, the next five grids are the AGs, each with a potential difference of 200 kV (total 1.009 MV). The total current foreseen for the ITER accelerator is 40 A of accelerated negative ions at a final kinetic energy of $E_0 \simeq 1$ MeV (beam power of 40 MW). Consequently, such a high energy-high current accelerator may be subject to a non-negligible heat load to the grids by secondary particle impacts.

A. Negative ion induced secondary emission

In order to estimate power deposition and current on grids induced by secondary particles, we calculate the potential and magnetic field map inside the accelerator. In the following simulations, the potential map is calculated using SLAC-CAD [8]. The magnetic fields have different origins, namely (i) generated by a set of permanent SmCo magnets on the ion source, (ii) from a high current flowing through the PG grid (typically $\simeq 4$ kA for the MAMuG design), and (iii) from a set of permanent magnets embedded inside the EG grid. The effect of the magnetic field from the ion source magnets and that created by the PG current is to deflect electrons generated by stripping reactions and ionization of the background gas while, as explained earlier, the aforementioned fields and the EG field are to deflect coextracted plasma electrons and associated secondary electrons toward the EG grid. The magnetic fields are calculated numerically using the CIRIC code [9].

Furthermore, the typical design for the EG has a permanent magnet embedded between each hole in the grid with alternating polarization for one hole to the next. The alternating polarization means that the simulation domain in EAMCC has to include two adjacent beamlets to properly describe all the particle trajectories. This is done as follows: a macroparticle is allowed to cross two holes (each with the correct EG magnetic field, i.e., alternating in direction). A macroparticle leaving the calculation domain into what would be a neighboring hole is reinjected symmetrically into the domain.

Last, for the calculations presented here, it is assumed that a uniform negative deuterium current density is extracted from the plasma source through the 1280 holes of the PG.

In this section, we estimate the power deposition and current flowing through MAMuG grids induced by the byproducts of collisions between the extracted negative ions and the residual background gas. The latter originates mainly from the ion source. As explained above, the gas pressure in the source is assumed to be 0.3 Pa when no plasma is present in the source. The background gas density profile is calculated using a Monte-Carlo method [33], being more accurate than using a classical conductance approach [34]. Figure 7 shows the gas density profile for typical working conditions, that is, ion source gas temperature $T_g = 2000$ K and residual gas pressure from the neutralizer $P_N = 0.019$ Pa. Other relevant parameters for the MAMuG accelerator are PG current $I_{\mathrm{PG}} = 4$ kA, EG voltage $V_{\mathrm{EG}} = 9.4$ kV, and extracted negative deuterium ion current density $J_{\mathrm{D}} = 28.6\ \mathrm{mA/cm^2}$ (the latter ensure a 40 A accelerated current at the accelerator exit). The total

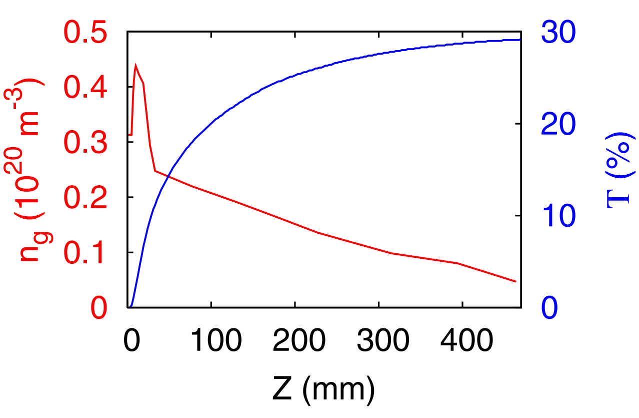

FIG. 7. (Color) Background gas density profile $n_g(z)$ and negative deuterium ion stripping rate $\Gamma(z)$ as a function of propagation distance inside the accelerator vessel. The gas profile is calculated using the Monte-Carlo method described in Ref. [33]. A filling pressure of 0.3 Pa in the ion source is assumed (with no source operation and the system at room temperature) together with a residual pressure from the neutralizer $P_N = 0.019$ Pa and a source gas temperature $T_g = 2000$ K during discharge operation.

extracted D^- current is consequently found to be $I_D \simeq$ 56.4 A (Note that the grid apertures are $R_{PG} = 7$ mm for the PG, $R_{EG} = 5.5$ mm for the EG, and $R_{AG} = 8$ mm for the AGs.) For a detailed description of the permanent magnet configuration in the ITER-MAMuG design see Refs. [1,4].

The total negative ion stripping loss is $\simeq 29\%$ (27.8% from single stripping reactions and 1.3% for double stripping, respectively) as shown in Fig. 7. The background gas ionization rate is about 6.1%. Consequently, the corresponding secondary electron current generated inside MAMuG accelerator is $I_e \simeq 20.5$ A; the latter represents the main fraction of high energy electrons. The other mechanisms for creating electrons are (i) true secondary electrons generated by electron and heavy particle impacts on grids and (ii) coextracted plasma electrons. As explained earlier, these electrons are accelerated by the electric field, deflected by the magnetic fields, and consequently will deposit power on the grids. Electrons are responsible for the majority of the grid power load (96% of total power). The total power deposition from electrons, $P^{(e)}_{\rm grid}$, is calculated to be 7 MW (including contribution from coextracted plasma electrons). The power transmitted toward the neutralizer by electrons is significantly smaller, $P^{(e)}_{\rm neut} \simeq 600$ kW (1.95 A). Total power deposition from electrons and heavy particles is summarized in Table III.

Stripping reactions (see Table II) produce a large number of neutrals ($\simeq 28\%$). These neutrals are mostly transmitted toward the neutralizer (2.2 MW) and a negligible amount of power is deposited on grids. Neutral impacts with grids are essentially from the ones created between the plasma grid (PG) and the back of the extraction grid (EG). They are consequently low energy, i.e., typically $E_0 \lesssim 50$ keV.

Positive ions (D^+ and D_2^+) generated inside the accelerator usually go back towards the plasma source. The total power carried by these heavy particles is about 880 kW (3.2 A) at the entrance of the PG with a high maximum power density $\mathcal{P}_{\rm max} \simeq 2.5\ {\rm kW/cm^2}$. The corresponding power density profile is shown in Fig. 8. The aperture in the PG acts on the positive ion beam as a converging lens

TABLE III. Total power generated by secondary particles in MAMuG calculated by the EAMCC code. $P_{\rm grid}$ corresponds to the total power deposited on grids, $P_{\rm neut}$ power transmitted toward the neutralizer, and $P_{\rm src}$ back into the negative ion source. The numbers shown include contribution from (i) stripping reactions, (ii) ionization of background gas, and (iii) coextracted plasma electrons.

	$P_{\rm grid}$ (MW)	$P_{\rm neut}$ (MW)	$P_{\rm src}$ (MW)
e^-	7	0.6	None
D^0	0.1	2.2	None
D^+	Negligible	Negligible	0.14
D_2^+	0.13	None	0.74

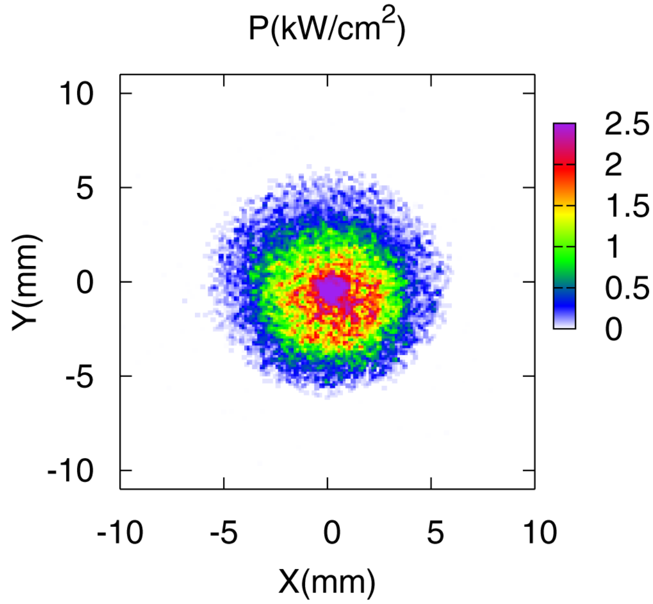

FIG. 8. (Color) Power density profile associated with one positive ion beamlet going back toward the ion source. The plot shows the contribution from all positive ion species at the entrance of the plasma grid. The total power carried by the beamlets in the ITER-MAMuG accelerator is found to be $P_{\rm tot} =$ 880 kW.

and consequently the maximum power density increases as a function of propagation distance inside the ion source. Typically, we have $\mathcal{P}_{\rm max} \simeq 4\ {\rm kW/cm^2}$, 20 cm from the PG, and $\mathcal{P}_{\rm max} \simeq 6\ {\rm kW/cm^2}$ at 40 cm. This obviously may have negative consequences on the back side of the ion source and must be considered carefully.

Figure 9(a) shows the power deposited on each grid individually. We address for now the case of an ideal beam and the consequences of a beamlet halo will be discussed in the next section. Most of the power and current to the EG comes from the coextracted plasma electrons. The AGs, on the contrary, are heated by secondary particles which are by-products of collisions between the accelerated negative ions and the background gas. A great fraction of the total negative ion loss occurs in the first 100 mm of the accelerator, between the PG and first AG, as demonstrated in Fig. 7, due to the high concentration of residual gas. Consequently, the vast majority of the created secondary particles are collected by the second and third AGs (an illustration of particle trajectories may be seen in Fig. 6). It should be noted, as explained before, that due to the low mass of electrons compared to ions, most of secondary electrons are deflected onto the grids, whereas ions are mostly transmitted out of the accelerator, hence most of the power to the grids comes from electron impacts.

Note that the total power may be as high as $\simeq 4.5\%$ of the accelerated deuterium beam power (40 MW) for AG 2

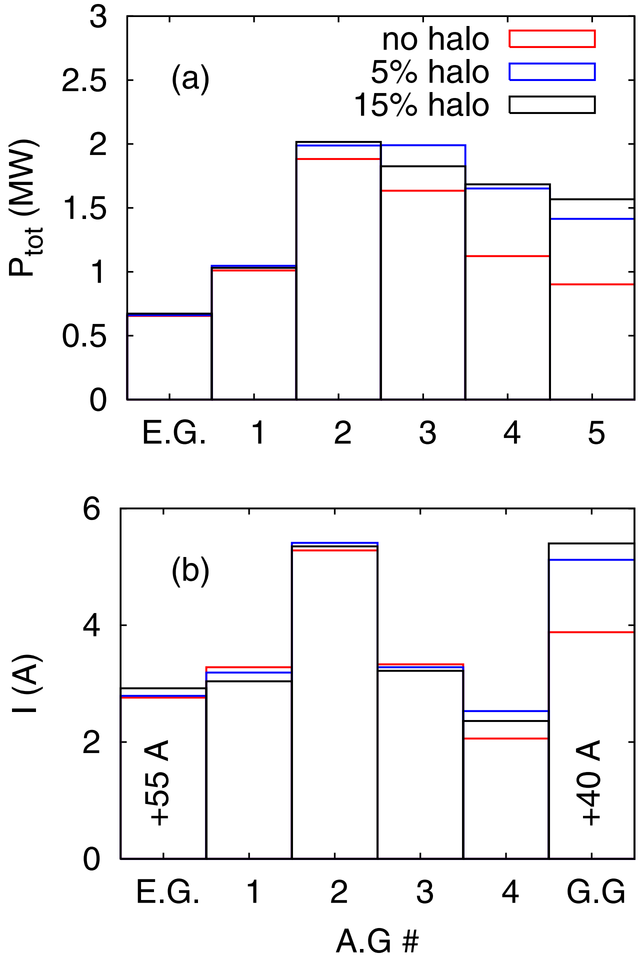

FIG. 9. (Color) (a) Total power deposition and (b) total current flowing into accelerator grids. Three distinct cases are shown: (red color) power and current deposition produced in ideal working conditions, i.e., no beamlet halo; (blue color) power and current deposition including a halo with a current representing 5% of the total accelerated beam current transmitted toward the neutralizer (which is 40 A); and last (in black), power and current deposition including a halo with a current representing a 15% halo. Label "G.G" stands for grounded grid. The total current measured at G.G is the so-called drain current, which is the total current collected at ground potential inside the neutral beam injector.

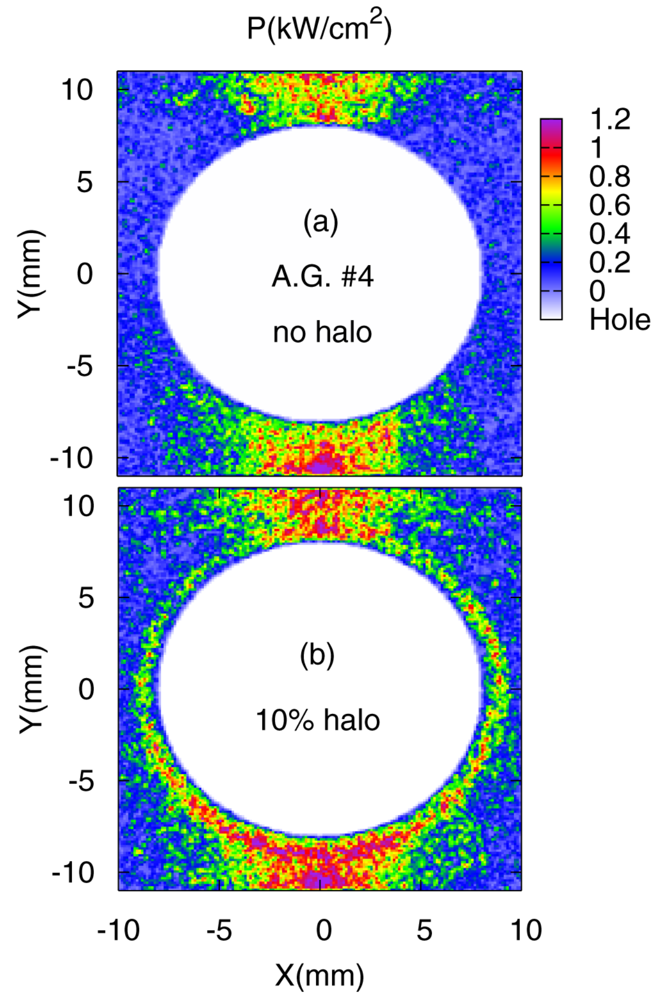

FIG. 10. (Color) Power density profile on the front face of AG 4 induced by secondary particle impacts. (a) shows the case of beamlets without halos and (b) assuming a transmitted halo current equivalent to 10% of the total accelerated negative ion beamlet current, corresponding to $I_D^{\rm halo} = 4$ A for the ITER-MAMuG example. The maximum power density is found to be of the order of 2.5 kW/cm^2.

(with no beamlet halo). In addition, the maximum power density is found to be in the range 1.2–2.5 kW/cm^2 for all the grids. As an example, Fig. 10(a) shows the power density profile on the front face (i.e., that facing the ion source) of the fourth AG assuming negative ion beamlets without halos.

Figure 9(b) plots the total current flowing through the accelerator grids. The grounded grid measures the drain current, which is the total current collected at ground potential inside the neutral beam injector as a whole. This current includes the particles flowing into the last accelerator grid (AG 5) as well as all other transmitted particles hitting the injector walls downstream of the electrostatic accelerator, including the 40 A of the D^- beam. The electron current measured at the EG is also split into two parts for clarity purposes. The current shown in Fig. 9(b) corresponds to the one produced by the by-products of stripping and ionization reactions. The additional 55 A mentioned is associated with the coextracted plasma electrons collected by the EG.

B. Power deposition induced by beamlet halos

The ITER requirement of producing 40 A of negative deuterium ion current implies the extraction of a higher current from the negative ion source due to the high stripping losses inside the accelerator vessel. For the ITER-MAMuG design, which has a PG grid with 1280 apertures

(14 mm in diameter), we calculated an extracted current density $J_D = 28.6\ \mathrm{mA/cm^2}$ as reported in Sec. III A. Production of a high ion current implies the use of cesium inside the ion source in order to enhance the surface production on the PG grid, which occurs because cesium lowers the work function of the PG surface [6]; then neutrals, and to some extent positive ions from the source plasma, may trap electrons from the PG valence band during impact and be reflected back into the plasma as negative ions. This reaction can be highly efficient and allows the production of a large numbers of negative ions [35–39].

It has been found experimentally that accelerated negative ion beamlets do not have a pure Gaussian current density profile, but that they are better described by a bi-Gaussian profile [7]. The fraction of the beam with the larger divergence is referred to here as the beamlet halo. It is possible that the beamlet halo is formed by negative ions created on the downstream surface of the PG. Cesium will migrate from the ion source to the back of the PG and some of the D^0 atoms flowing out of the source will be reflected off surfaces and hit the downstream side of the PG and be backscattered as negative ions. Here it is assumed that negative ions formed on the rear side of the PG in an annulus around the hole are the source of the beamlet halo.

For the calculations discussed in this section, we keep the total accelerated negative ion beam current constant at 40 A, with an assumed halo fraction. The halo fraction is defined as follows: a 10% halo means that 10% of the total beam current existing the accelerator is carried by the halo, i.e., a halo current transmitted toward the neutralizer of 4 A. The remaining 36 A correspond to the accelerated low divergence beam extracted from the plasma source. It should be further noted that a halo will modify the beam optics.

Figure 9 shows the enhancement in power and current to the grids when a beamlet halo is present. A clear increase in total magnitude for both power and currents is calculated. The last three AGs experience the highest increase. The two distributions change when the halo is present, see Figs. 9(a) and 9(b). This arises because a large fraction of the negative ions forming the halo hits the grids, the rest is transmitted toward the neutralizer, but this does not necessarily reflect in the current to the grids as they can produce a large number of secondary electrons, which are collected further downstream. Consequently, there can be a reduction in current for a given grid but not in power deposition.

The total power deposition by beamlet halos is not negligible. We estimate an increase of the order of 1.65 MW on grids for a 15% halo and 1.55 MW for a 5% halo. The small difference between 5% and 15% halos may be explained from the fact that halo current does change significantly the beam optics inside the accelerator. The EG typically generates a strong focusing of beamlet halos, which in turn, due to its enhanced charge density, induces a space charge blowout of the low divergence beamlets extracted from the plasma source. This implies an overall lower charge density for the low divergence beams and consequently a lower magnitude space charge force on the beamlet halos. The direct consequence of this effect is that the larger the extracted halo current, the smaller is the amount of halo particles impacting the grids, i.e., there is a better transmission toward the neutralizer. We typically find a total impact ratio of $\simeq 27\%$ of the extracted halo current for a 5% beamlet halo, $\simeq 19\%$ impact ratio for a 10% halo, and last $\simeq 11\%$ impact ratio for a 15% halo.

Figure 10(b) shows the power density profile induced by secondary particle impacts on the front face of AG 4 with a 10% halo. The maximum power density does not increase significantly compared to the ideal case, see Fig. 10(a), and it remains in the range $\mathcal{P}_{\max} \simeq 2.5\ \mathrm{kW/cm^2}$.

C. Coextracted plasma electrons

As explained earlier, electrons may be extracted from the ion source together with the negative deuterium ions. In the ITER type plasma sources, we may expect as many as one electron per extracted ion [11,12]. This translates to an electron current density on the order of $J_e \simeq 28.6\ \mathrm{mA/cm^2}$ for the ITER-MAMuG design. Coextracted plasma electrons are typically collected by the EG and are responsible for the majority of the heat load on that grid.

In the simulations performed with EAMCC, we neglected space charge effects induced by the extracted electron beam when calculating the electrostatic field map inside the accelerator vessel (using the SLAC-CAD code [8]). This may be explained as follows: assuming an infinitely long cylindrically symmetric electron and ion beamlet and further neglecting relativistic effects (i.e., no self magnetic field generation), the space charge electric field, which has only a radial component, is found to be (for a detailed discussion on space charge, see [40])

$$E^{\mathrm{sc}}_{r,i} = \begin{cases} \frac{\rho_i r}{2\epsilon_0}, & \text{for } r < R \\ \frac{\rho_i}{2\epsilon_0}\frac{R^2}{r}, & \text{otherwise,} \end{cases} \tag{17}$$

where index i denotes either electrons or deuterium ions, ρ_i is the charge density, assumed constant (flattop profile), R is the beamlet radius and r the radial location. Clearly the ratio of space charge forces depends only on the ratio of charge densities, that is, expressed in terms of currents,

$$\frac{\rho_e}{\rho_D} \simeq \frac{J_e}{J_D}\sqrt{\frac{m_e}{m_D}}, \tag{18}$$

if we further assume similar extraction kinetic energies for both species, i.e., $E_0^{(\mathrm{e})} \simeq E_0^{(\mathrm{D})}$. Consequently, for $J_e \simeq J_D$ we have $\rho_e \ll \rho_D$ and electron space charge may be neglected.

Figure 11 shows the power density profile on the front face of the EG induced by coextracted plasma electrons and associated secondary particles for the ITER-MAMuG example. The extraction potential is currently set in the simulation to $V_{EG} = 9.4$ kV. The total power deposited on the EG is found to be $P_{tot} \simeq 520$ kW (including inside the hole and back side) from coextracted electrons while the contribution from stripping and ionization reactions is significantly lower, that is, $P_{tot} \simeq 135$ kW (including $P_{bck} \simeq 35$ kW on the back side essentially from positive ions). Furthermore, Fig. 11 shows the existence of a high power density region, with a maximum $\mathcal{P}_{max} = 1.1\ \mathrm{kW/cm^2}$. It should be noted that, due to the specific configuration of the static magnetic field in the extraction region with alternating magnet polarization from one hole to the next along the (Oy) direction, the high power density area jumps symmetrically from left to right.

Concerning transmission, only a small fraction of coextracted electrons are transmitted through the EG downstream of the accelerator. We estimate around 1.6% past the EG and down to 0.6% through AG 1, meaning 55 A of electrons are collected by the EG. Transmitted electrons, even if they represent a small fraction, still carry a non-negligible power. The total power carried by these particles amounts to $P_{tr} \simeq 275$ kW which is almost totally collected by the grids (a negligible power is transmitted toward the neutralizer).

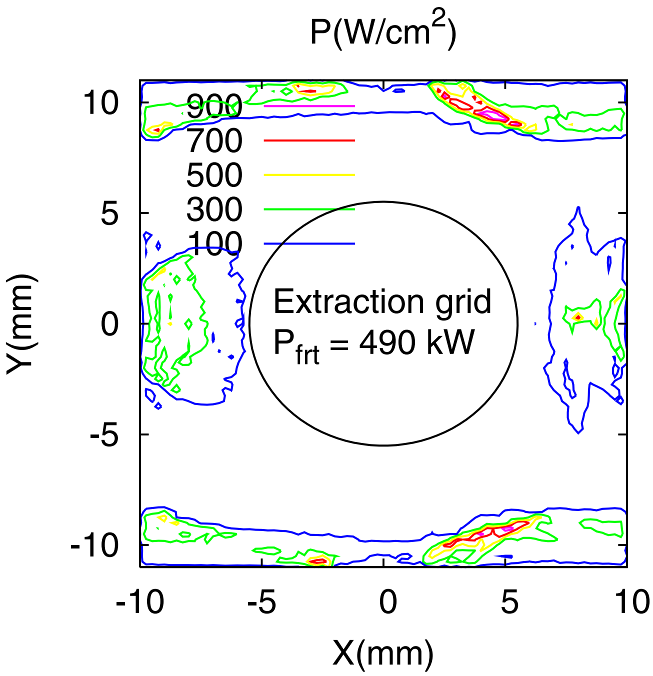

FIG. 11. (Color) Power density profile (contour plot) on the front face of the extraction grid induced by coextracted plasma electrons and associated secondary particles. The maximum power density is found to be $\mathcal{P}_{max} = 1.1\ \mathrm{kW/cm^2}$. Total power deposited on the grid is $P_{tot} = 520$ kW (including inside the hole and the back side of the grid) and $P_{frt} = 490$ kW in the front face. A 1.56% ratio of the electrons arriving at the grid is transmitted through the grid to the first acceleration gap.

IV. CONCLUSION

In this paper, we have developed a Monte-Carlo method suitable for studying secondary emission processes in typical electrostatic accelerators designed for heavy ion acceleration. We have applied the method to the calculation of power-current deposition inside the negative deuterium ion based accelerator for a future neutral beam injector of the ITER tokamak. In the code, secondary emission processes such as negative ion stripping reactions, ionization of the background gas, electron/heavy ion/neutral backscattering of grids, and true secondary electron emission are included. In addition, the code allows for a precise characterization of 3D power deposition and consequently the determination of high power density areas on accelerator grids, which makes it a useful tool for design purposes. In ITER-MAMuG accelerator the vast majority of power deposition on grids is induced by electrons (typically $\simeq 96\%$ of total power), which amounts to an integrated power (summed over all accelerator parts) close to 15.5% of the accelerated negative ion power (40 MW, i.e., 40 A at 1 MeV).

Power transmitted outside the accelerator is mostly carried by heavy particles and is found to be also non-negligible. A total power on the order of 880 kW is found for the positive ion beamlets going back toward the ion source together with a high maximum power density ($6\ \mathrm{kW/cm^2}$ at 40 cm downstream inside the plasma source). This may be a critical issue regarding cooling of the ion source walls. Note that the PG hole acts as a converging lens for the positive ion beams. Power transmitted toward the neutralizer is mostly carried by neutrals (2.2 MW) and is well collimated.

Last, additional power may come from the existence of a beamlet halo. The latter will induce direct fast heavy ion impact with grids and injector parts further downstream together with an increased load of true secondary electrons (heavy ion impacts may produce a high number of secondary electrons).

[1] T. Inoue *et al.*, Fusion Eng. Des. **56–57**, 517 (2001).
[2] ITER Physics Basis Editors, ITER Physics Expert Group Chairs and Co-Chairs, ITER Joint Central Team and Physics Integration Unit, and ITER EDA, Nucl. Fusion **39**, 2137 (1999).
[3] R. S. Hemsworth and T. Inoue, IEEE Trans. Plasma Sci. **33**, 1799 (2005).
[4] K. Watanabe, Y. Fujiwara, M. Hanada, M. Kashiwagi, T. Kitagawa, K. Miyamoto, T. Morishita, Y. Okumura, T. Takayanagi, and M. Taniguchi, Rev. Sci. Instrum. **71**, 1231 (2000).
[5] V. Vahedi and M. Surendra, Comput. Phys. Commun. **87**, 179 (1995).
[6] W. G. Graham, in *Proceedings of the Second International Symposium on the Production and Neutralization of Negative Hydrogen Ions and Beams*, edited by T.

Sluyters (Brookhaven National Laboratory, Upton, New York, 1980), p. 126.
[7] H. P. L. de Esch (private communication).
[8] J. Pamela, Rev. Sci. Instrum. **62**, 1163 (1991).
[9] D. Ciric (private communication).
[10] J. D. Jackson, *Classical Electrodynamics* (Wiley, New York, 1998).
[11] R. Trainham, C. Jacquot, D. Riz, A. Simonin, K. Miyamoto, Y. Fujiwara, and Y. Okumura, Rev. Sci. Instrum. **69**, 926 (1998).
[12] E. Speth *et al.*, Nucl. Fusion **46**, S220 (2006).
[13] T. Koshikawa and R. Shimizu, J. Phys. D **6**, 1369 (1973).
[14] T. Matsukawa, R. Shimizu, and H. Hashimoto, J. Phys. D **7**, 695 (1974).
[15] E. H. Darlington, J. Phys. D **8**, 85 (1975).
[16] E. J. Sternglass, Phys. Rev. **95**, 345 (1954).
[17] M. A. Furman and M. T. F. Pivi, Phys. Rev. ST Accel. Beams **5**, 124404 (2002).
[18] P.-F. Staub, J. Phys. D **27**, 1533 (1994).
[19] M. B. E. Bruining, *Physics and Applications of Secondary Electron Emission* (Pergamon Press, New York, 1954).
[20] Y. F. Chen, J. Phys. D **28**, 2163 (1995).
[21] E. W. Thomas, Oak Ridge National Laboratory, Technical Report No. ORNL-6088, 1985.
[22] A. M. D. Assa'd and M. M. E. Gomati, Scanning Microsc. **12**, 185 (1998).
[23] P. J. Ebert, A. F. Lauzon, and E. M. Lent, Phys. Rev. **183**, 422 (1969).
[24] K. A. Wright and J. G. Trump, J. Appl. Phys. **33**, 687 (1962).
[25] L. Wang, Y. Y. Lee, G. Mahler, W. Meng, D. Raparia, J. Wei, and S. Henderson, Phys. Rev. ST Accel. Beams **8**, 094201 (2005).
[26] V. Baglin, I. Collins, B. Henrist, N. Hilleret, and G. Vorlaufer, CERN, Technical Report (LHC Project Report) No. 472, 2002.
[27] B. Henrist, N. Hilleret, M. Jimenez, C. Scheuerlein, M. Taborelli, and G. Vorlaufer, CERN, Technical Report (Yellow Report) No. CERN-2002-001, 2002.
[28] C. F. Barnett, Oak Ridge National Laboratory, Technical Report No. ORNL-6086, 1990.
[29] Y. M. Fogel, A. G. Koval, Y. Z. Levchenko, and A. F. Khodyachikh, Sov. Phys. JETP **12**, 384 (1961).
[30] B. Svensson and G. Holmén, Phys. Rev. B **25**, 3056 (1982).
[31] R. A. Baragiola, E. V. Alonso, and A. O. Florio, Phys. Rev. B **19**, 121 (1979).
[32] W. Eckstein and F. E. P. Matschke, Phys. Rev. B **14**, 3231 (1976).
[33] A. Krylov and R. S. Hemsworth, Fusion Eng. Des. **81**, 2239 (2006).
[34] S. Dushman and J. M. Lafferty, *Scientific Foundations of Vacuum Technique* (Wiley, New York, 1962).
[35] K. N. Leung *et al.*, Rev. Sci. Instrum. **61**, 2378 (1990).
[36] J. W. Kwan *et al.*, Rev. Sci. Instrum. **62**, 1521 (1991).
[37] A. Ando, Y. Yakeiri, K. Tsummori, O. Kaneko, Y. Oka, R. Akiyama, T. Kawamoto, K. Minone, T. Kurata, and T. Kuroda, Rev. Sci. Instrum. **63**, 2683 (1992).
[38] Y. Okumura, M. Hanada, T. Inoue, H. Kojima, Y. Matsuda, Y. Ohara, M. Seki, and K. Watanabe, in *Proceedings of the Fifth International Symposium on the Production and Neutralization of Negative Hydrogen Ions and Beams*, edited by A. Hershcovitch, AIP Conf. Proc. No. 210 (AIP, New York, 1990), pp. 169–183.
[39] M. Hanada, T. Inoue, M. Mizuno, Y. Ohara, Y. Okumura, Y. Suzuki, H. Tanaka, M. Tanaka, and K. Watanabe, Rev. Sci. Instrum. **63**, 2699 (1992).
[40] G. Fubiani, J. Qiang, E. Esarey, W. Leemans, and G. Dugan, Phys. Rev. ST Accel. Beams **9**, 064402 (2006).